Investigation of the impact of additive manufacturing techniques on the acoustic performance of a coiled-up resonator

Investigation of the impact of additive manufacturing techniques on the acoustic performance of a coiled-up resonator

Gioia Fusaro[1a)], Luca Barbaresi[1], Matteo Cingolani[1], Massimo Garai[1], Edoardo Ida[1], Andrea Prato[2], Alessandro Schiavi[2]

[1] *Department of Industrial Engineering, University of Bologna, Viale Risorgimento 2, Bologna, 40136, Italy*

[2] *INRiM – National Institute of Metrological Research, Division of Applied Metrology and Engineering, Torino, Italy*

Acoustic metamaterials (AMM) offer innovative solutions for physics and engineering problems, allowing lighter, multiphysics and sustainable systems. They are usually studied analytically or numerically and then tested on prototypes. For this reason, additive manufacturing (AM) techniques are a popular way of quickly realising AMMs' innovative geometrical designs. However, AM parameters are often standardised without considering the specific issues of each AMM geometrical shape, leading to a possible mismatch between the analytical (or numerical) and experimental results. In this study, a simple AMM - a coiled-up resonator – has been produced with different AM technologies (fused deposition modelling, FDM, stereolithography, SLA, and Selective Laser Melting, SLM) and materials (PLA, PETG, resin, flexible resin and stainless steel,). The sound absorption performance of these samples has been measured in two research labs in Italy and compared with the analytical and numerical calculations. This permitted the identification of the best combinations of AM technologies, their set-up, and materials matching the expected results. The SLA/Resin combination performed better overall; however, cheaper and more easily manageable samples made with FDM and PETG can achieve the same acoustic performance through the optimal AM printing set-up. It is expected that this methodology could also be replicated for other AMMs. [https://doi.org(DOI number)]
[XYZ] Pages: 1-12

I. INTRODUCTION

Acoustic metamaterials have become a resourceful method for designing systems that allow an effective alternative to conventional sound insulating (Lu et al., 2020; Wang et al., 2016; Melnikov et al., 2020), absorbing (Chen et al., 2020; Cingolani et al., 2022b; Jiménez et al., 2016; Shao et al. 2021) and diffusing materials (Jimenez et al., 2017; (Jimenez et al., 2017; Varanasi et al., 2017; Pilch, 2021; Zhu et al., 2017).

The control of sound absorption and sound reflections, particularly at low frequencies or at specific narrow frequency bands (generally requiring the use of bulky materials or systems), can be achieved by exploiting peculiar small-size shaped resonant structures and cavities, such as a coiled-up resonator. Specifically, a coiled-up resonator is a classical Helmholtz resonator (as described in 1863 (Helmholtz, 1863)) with an elongated shaped-designed cavity. Such geometrical configuration allows the coiled-up resonator to force an incident field of elastic waves (such as sound pressure or vibration) to behaviour not otherwise found in nature or beyond what is possible with conventional materials by extending the concept of a material (Sutton, 2021) and by enhancing its properties (Alomarah et al., 2022). In that meaning, a coiled-up resonator can be considered an 'acoustic metamaterial' (or an 'acoustic metasurface' unit-cell (Assouar et al., 2018)), being an artificially structured material ("Encyclopedia Britannica," n.d.), engineered with the proper shape, geometry, size, orientation and periodic arrangement.

Such structures are particularly suited to additive manufacturing (AM) processes, i.e. fused deposition modelling (FDM), ceramic powder, Stainless Steel powder, and stereolithography (SLA)(Franco-Martínez et al., 2022; Kennedy et al., 2019; Morris et al., 2018; Zieliński et al., 2020). In previous research, the authors have proved that the acoustic performance of FDM PolyEthylene Terephthalate Glycol-modified (PETG)-based coiled-up resonators depends on the geometrical parameters' variation, which is influenced by thermal conditions: temperature variations cause thermal deformations of the spiral length and hole diameter (Cingolani et al., 2022a), inducing a frequency shift of main peaks that follows an exponential trend (Cingolani et al., 2022a). However, the influence of the 3D printing set-up and quality on the physical performance of coiled-up resonators is yet to be defined. For this reason, three prototyping methods and five constitutive materials have been analysed in this study to define which one better approximates the expected acoustic response (as per analytical and numerical provisional studies).

The present parametric and comparative investigation

[a]gioia.fusaro@unibo.it

aims to determine if, for the coiled-up resonators, there could be an optimal configuration of AM techniques and material that could better approximate the analytical and numerical designed result. First, an analytical investigation following Cai et al. (Casarini et al., 2018) coupled with a Finite Elements Method (FEM) analysis in measurement-like conditions provided a provisional first absorption coefficient result. Secondly, a series of AM techniques (FDM, SLA, and Selective Laser Melting, SLM) and 3D printing materials (filament, resin, or powder) was used to produce the coiled-up resonator with various 3D printing set-ups. Finally, two impedance tubes (one in the Italian National Metrology Institute, also known as INRIM, and another one in the University of Bologna laboratories) were used to test the absorption coefficient of each AM set-up and material. Once the results highlight a best practice for this prototype, the same mixed methodology could also be replicated for other AMMs.

II. METHODS

A. Analytical method for coiled-up resonators characterisation

Among sound absorbers based on the Helmholtz resonance principle, coiled-up resonators have been widely used due to their tenability and suitability for metasurfaces applications(Magnani et al., 2022; Yu et al., 2019). For this reason, they were selected in this research to investigate the accuracy of different 3D printing materials and methods in reproducing the expected analytical and numerical results. Specifically, the geometrical model of coiled-up resonators that will be used has already been discussed in a previously published paper(Cingolani et al., 2022a).

Figure 1 (Colour online) View of the circular specimen with embedded coplanar spiral tube obtained with the slow-fine manufacturing setting. The overall thickness of the specimen is 11.1 mm, the diameter of the sample is $2R_0$ = 39 mm, the side of the hole square is 2a = 5.59 mm, the porosity of the front panel is ϕ = 2.6%, the total spiral length is L_t = 133 mm.

The spiral tube length (L_t), the side of the square perforation (2a) and the radius of the circular specimen (R_0) are the geometric constitutive parameters of the investigated coiled-up resonators (see *Figure 1*). Concerning ducts with a rectangular section, the general solution of the two-dimension wave equation is found through the definition of the two-dimension wave equation is found through the definition of two parameters(Stinson and Champoux, 1992):

$$\alpha_k = \left(k+\frac{1}{2}\right)\pi/a \quad \beta_n k = \left(n+\frac{1}{2}\right)\pi/b \tag{1}$$

where *a*, *b* are the half-width and the half-height of a rectangular cross-section, and *k*, *n* are the indexes of all the terms that satisfy the boundary conditions. The effective density, $\rho(\omega)$, and the compressibility, $C(\omega)$, are constitutional wave variables of the tube, and can be defined according to visco-thermal acoustic theories(Stinson and Champoux, 1992):

$$\rho(\omega) = \rho_0 \frac{a^2 b^2}{4i\omega}\left(\sum_{k=0}^{N}\sum_{n=0}^{N}\left[a_k^2 b_n^2\left(a_k^2+b_n^2+\frac{i\omega}{v}\right)\right]\right)^{-1} \tag{2}$$

$$C(\omega) = \frac{1}{P_0}\left[1-\frac{4i\omega(\gamma-1)}{v' a^2 b^2}\left(\sum_{k=0}^{N}\sum_{n=0}^{N}\left[a_k^2 b_n^2\left(a_k^2+b_n^2+\frac{i\omega\gamma}{v'}\right)\right]\right)^{-1}\right] \tag{3}$$

with ρ_0 being the air density, v the air kinematic viscosity, P_0 the equilibrium pressure of the air, v' the air thermal diffusivity, and γ the heat capacity ratio in air. Therefore, the characteristic impedance is derived as a function of the effective density and the compressibility:

$$Z_c(\omega) = \sqrt{\frac{\rho(\omega)}{C(\omega)}} \tag{4}$$

The resulting acoustic impedance at the entrance of a tube with rigid termination is(Cai et al., 2014):

$$Z_t(\omega) = -iZ_c(\omega)\cot(kL_t) \tag{5}$$

where $k^2 = -\omega^2\rho C$ is the effective propagation constant. Following these definitions, the input-specific acoustic impedance of sound waves for the coiled-up resonators is:

$$Z_{in} = \frac{Z_t}{\phi} = \frac{Z_t}{\frac{(2a)^2}{\pi R_0^2}} \tag{6}$$

where ϕ is the porosity of the specimen, which is defined as the ratio between the surface area of the square perforation (a^2) and the surface area of the circular specimen (πR_0^2). The relationship between the input-specific acoustic impedance and the normal incidence sound absorption coefficient, α_n, is the following:

$$a_n = 1 - \left|\frac{Z_{in}-\rho c}{Z_{in}+\rho c}\right|^2 \tag{7}$$

where ρc is the characteristic impedance of air.

B. Numerical method

In order to assess the analytical results and implement the metamaterial geometry through parametric sweeps, numerical models are frequently used (Cingolani et al., 2022a; Fusaro et al., 2020). In this study, the commercial software Comsol Multiphysics was used for this aim in order to set up a reference α-value in reference conditions (T = 20 °C). For this reason, the numerical model followed up a calibration based on experimental α_n values in the whole frequency spectrum considered at T = 20 °C (pressure acoustics, frequency domain module).

The input mesh of each model included three different domains: the geometry corresponding to the 3D printed specimen (characterised by each material properties), the inner volumes within resonators (air material properties), and the air volume of the impedance tube (air material, plane wave radiation). A schematic of the geometry and the boundary conditions is presented in Figure 2. The exact geometry of the coplanar spiral tube was reproduced to consider the curved parts' effects (Cai et al., 2014). In order to reproduce the experimental impedance tube's transfer-function method, the boundary conditions of the numerical model are characterised by plain wave radiation at the opposite side of the impedance tube with respect to the coiled-up resonator (to simulate the loudspeaker) with a prescribed sound pressure amplitude of 1 Pa. Furthermore, all the geometry is characterised as sound hard boundary conditions imposing null displacements along the axial direction concerning the tube. Finally, the mesh size has been defined through the standard FEM criterion for acoustic models to obtain at least six elements for the smallest wavelength, considering the maximum frequency of 4000 Hz, according to convergence recommendations (Marburg and Nolte, 2008).

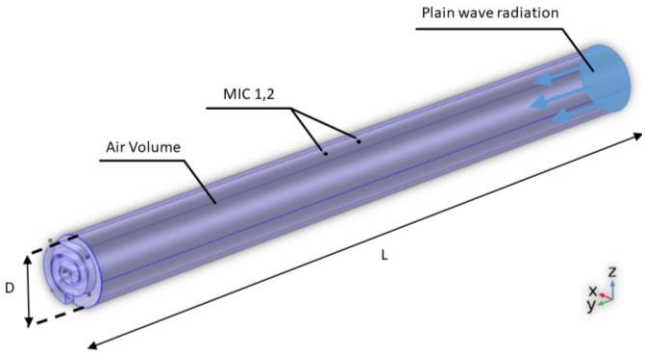

Figure 2 (Colour online) Schematic of the geometry and the boundary conditions

C. Acoustic absorption coefficient experimental measurements – Laboratory A and B

The impedance tubes used in the study are placed in the Italian National Metrology Institute (INRIM) and the Industrial Engineering Department of the University of Bologna, respectively, addressed in this study as Lab A and Lab B. Lab A circular impedance tube is made of Plexiglas to guarantee rigid, smooth, non-porous walls, with 50 mm internal diameter and 650 mm length, with two ¼" B&K 4136 microphones adopted for sound pressure measurement. The microphone spacing is fixed at 26 mm; thereby, the absorption coefficient α_n is limited at the precautionary frequency range of 100 Hz – 4000 Hz. Microphones can rotate 180° as required in ISO 10534-2 for instrument calibration (*ISO 10534-2: 1998. Acoustics – Determination of sound absorption coefficient and impedance in impedance tubes – Part 2: Transfer function method*, 1998). A white noise, generated with a B&K 1405 noise and amplified by a B&K 2706 power amplifier, is emitted by a sound source connected to the tube. Microphones are pre-amplified by a B&K 2807 microphone power supply, and their signal is acquired by a NI 4431 board connected to a PC, processed in real-time through Labview NI "Sound and Vibration Toolbox" and post-processed with MATLAB. Measurements are carried out in a temperature-controlled laboratory between 20 °C and 23 °C. In Lab B's impedance tube, the roughness of the interior walls does not influence the experimental measurements, as calibration with an empty tube is performed every month as required in ISO 10534-2 for instrument calibration(*ISO 10534-2: 1998. Acoustics – Determination of sound absorption coefficient and impedance in impedance tubes – Part 2: Transfer function method*, 1998). A rigid ring adapter is used to fit the 40 mm diameter coiled-up resonator into the 50 mm diameter impedance tube. Modelling clay around the contact edge between the two is placed so no gaps are left.

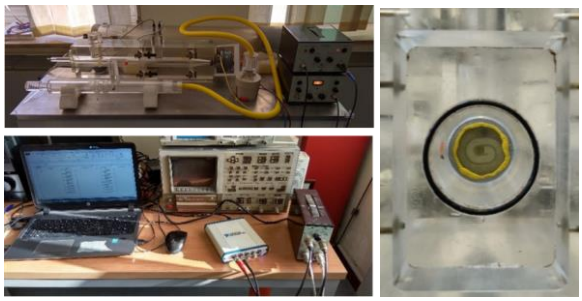

Figure 3 INRiM (Lab A) impedance tube measurement set-up conditions (T = 20 °C). For this reason, the numerical model followed up a calibration based on experimental α_n values in the whole frequency spectrum considered at T = 20 °C (pressure acoustics, frequency domain module).

The input mesh of each model included three different domains: the geometry corresponding to the 3D printed specimen (characterised by each material properties), the inner volumes within resonators (air material properties), and the air volume of the impedance tube (air material, plane wave radiation). A schematic of the geometry and the boundary conditions is presented in Figure 2. The exact geometry of the coplanar spiral tube was reproduced to consider the curved

parts' effects (Cai et al., 2014). In order to reproduce the experimental impedance tube's transfer-function method, the boundary conditions of the numerical model are characterised by plain wave radiation at the opposite side of the impedance tube with respect to the coiled-up resonator (to simulate the loudspeaker) with a prescribed sound pressure amplitude of 1 Pa. Furthermore, all the geometry is characterised as sound hard boundary conditions imposing null displacements along the axial direction concerning the tube. Finally, the mesh size has been defined through the standard FEM criterion for acoustic models to obtain at least six elements for the smallest wavelength, considering the maximum frequency of 4000 Hz, according to convergence recommendations (Marburg and Nolte, 2008).

Lab B circular impedance tube is made of Plexiglas too, built according to ISO 10534-2 (*ISO 10534-2: 1998. Acoustics – Determination of sound absorption coefficient and impedance in impedance tubes – Part 2: Transfer function method*, 1998) and following the so-called one microphone method in order to prevent the mismatch between the two microphones. The impedance tube's diameter is 40 mm, and its operating frequency range is 300 - 5000 Hz. The measurements chain consists of a loudspeaker for signal generation, a signal amplifier (Samson 120A with SNR = 96 dB), an audio device, a single microphone ¼" PCB and a signal conditioner PCB Model 482C15. The output signal from the loudspeaker is an exponential sine sweep(Corredor-Bedoya et al., 2021) converted to an analogue signal by the DAC of the soundcard (RME 802). The pressure signals recorded by the microphone are converted to digital audio objects through the Analog-to-Digital Converter and sampled with a sample rate of 44.1 kHz at 24-bit depth, avoiding dynamic gain issues. The digital signal processing was developed with MATLAB software(Matlab, 2019) exploiting the ITA- Toolbox Impedance Tube calculation scripts(ITA-Toolbox, 2017), according to the Transfer-Function Method(Chung and Blaser, 1998). In Lab B's impedance tube, the roughness of the interior walls does not influence the experimental measurements, as calibration with an empty tube is performed before every measurement.

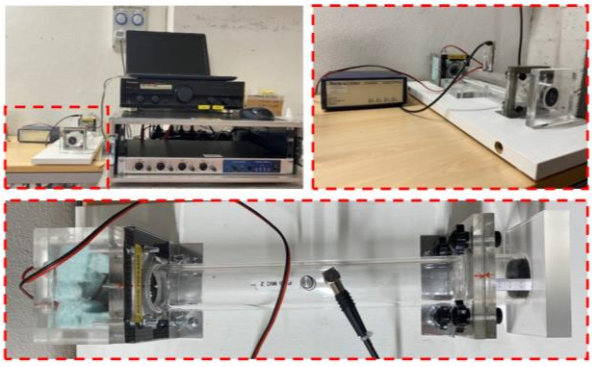

Figure 4 (Colour online) University of Bologna (Lab B) impedance tube measurement set-up

D. Roughness and Porosity experimental measurement

One potential influencing parameter that could imply a variation between analytical and numerical results with the experimental ones could be the roughness (R) derived by the 3D printing techniques and materials. The roughness of the different materials is measured with a Taylor Hobson Form Talysurf 120L roughness tester (see Figure 5). It uses direct contact of a diamond-tip stylus to the surface for measurement. The diameter of the tip is 4 μm, and the cone angle is 60°. With this system, it is possible to measure the main roughness amplitude parameters to characterise surface topography: the arithmetic average height of the profile (R_a), the maximum height (R_t) and the ten-point height (R_z) according to ISO 21920-2:2021 (Standardization, 2021) and DIN 4768:1990 (Gadelmawla et al., 2002).

Moreover, a qualitative study on the coiled-up resonator internal wall was run through Scanning Electron Microscopy (SEM) technology to define the characterisation derived from different Printing Velocity and Quality parameters. The SEM microscope used is a SEM Zeiss EVO 50 VP (EDS Oxford Instruments x-act), placed in the University of Bologna laboratory.

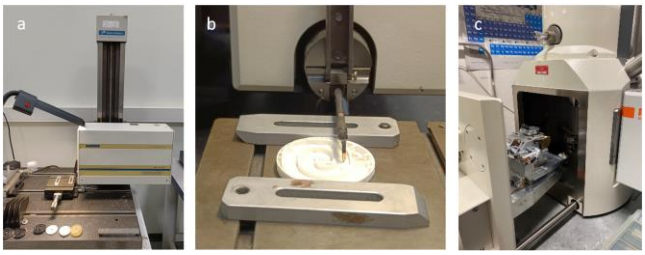

Figure 5 Taylor Hobson Form Talysurf 120L roughness tester ((a) general view and (b) application to a coiled-up sample), and (c) SEM Zeiss EVO 50 VP used for measuring the porosity.

E. Additive Manufacturing techniques and set-ups

Additive manufacturing is a reliable method widely used in the acoustic engineering research community (Johnston and Sharma, 2021; Kim and Yoon, 2021) through various techniques which are characterised by several 3D printing set-ups affecting the product (Askari et al., 2020; Kennedy et al., 2019). Five prototypes have been produced through Fused Deposition Modelling (FDM), Stereolithography (SLA), and Selective Laser Melting (SLM). In the first method, a specific material (PLA or PETG) filament is fused through a nozzle and deposited on the printing platform following specific geometry and layering inputs. In the second method (SLA), the liquid material (resin), constrained in a container, is polymerised through UV light following a specific geometry. Finally, the third method (SLM) generates a designed geometry by melting a stainless steel powder.

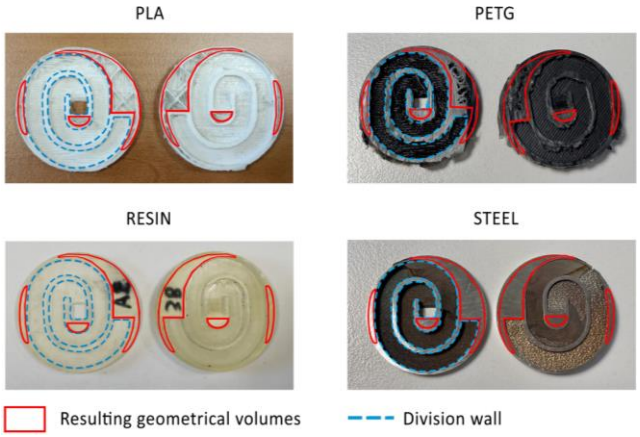

Figure 6 (Colour online) Photos of the sectioned 3D printed prototypes in FDM-PLA, FDM-PETG, SLA-Resin, and SLM-Stainless Steel, cut in half to display the upper (left) and lower (right) sides. The filling density of the resulting geometrical volumes (marked with the red lines) and the resonant volume walls' (blue line) characterisation can be observed.

As highlighted from Figure 6 in this research, various combinations of printing settings are explored to assess the influence of the manufacturing process on the acoustic properties of the AMM geometry under study. The samples have been cut in half to appreciate the printing characterisation results, and the upper (left) and lower (right) sides are displayed in Figure 6. Specific attention should be addressed to the red highlighted area. These are the resulting volumes, defined as a volume within the prototype geometry that does not have a specific characterisation (e.g., the volume enclosed in a cylinder) and for which a filling density can be set up (with different degrees of customizability). According to the printing machines' limits, these volumes are characterised by different filling densities. Another important feature shown in Figure 6 is the inner division wall characterisation, which depends on the printing Speed and Quality of the printing machines' set-ups.

1. FDM Optimal set-up determination

Two of the specimens involved in the present work have been manufactured through FDM technology. FDM is one of the most widespread additive manufacturing technologies for various reasons (Allen and Trask, 2015)(Morris et al., 2018): the range of thermoplastic polymers that can be used as raw material for the process is extensive; recent advancements in raw-material (filament) production allows to exploit of recycled thermoplastic materials making this technology ecologically sustainable; FDM machines are generally affordable and of low maintenance costs. The printers used in this case to produce coiled-up resonators were Flashforge Creator 3 (for PETG) and MakerBot Replicator + (for PLA). Specifically, for the combination Flashforge Creator 3 and PETG, the speed parameters (Base speed, Outline speed, Solid layer speed and Infill speed) and quality parameters (number of top and bottom solid layers and layer height), have been involved in an optimisation process while maintaining other settings constant (see Table *1*). Given several circular features in the specimens, a higher speed usually produces less accurate curvilinear features; thus, the faster the process, the worst the specimen is expected to be. Flashforge Creator 3 can produce components by deposing 50 μm thick layers of thermoplastic material, with an 11 μm horizontal positioning resolution within a layer. Simple stepper motors drive the Cartesian mechanical architecture that displaces the extruder nozzle without feedback control on the position of the nozzle. Thus, the manufacturing processes' absolute accuracy is influenced by the printing material (some thermoplastic polymers exhibit severe shrinkage and deformation after extrusion) and by the print-process setup(Kuznetsov et al., 2018).

The material selected for the FDM optimal set-up determination was Formfutura HD-glass, an amorphous PETG. This filament was chosen for its appropriate mechanical properties (high tensile modulus and strength) and nearly deformation-free printing capabilities(Ligon et al., 2017). Two-speed settings were considered: a slow setting, characterised by a Base speed of 50 mm/s, an Outline speed of 15 mm/s, a Solid layer speed of 30 mm/s, and an Infill speed of 45 mm/s, and a fast setting, characterised by a Base speed of 80 mm/s, Outline speed of 25 mm/s, Solid layer speed of 50 mm/s, and Infill speed of 75 mm/s. The layer height is usually proportional to surface roughness; thus, the thinner the layers (compatible with the material used), the smoother the specimen surfaces. Therefore, two quality settings were investigated as well: the Fine and Coarse settings were respectively characterised by the Number of top and bottom solid layers of 4 and 2 and a Layer height of 0.12 and 0.30 mm. Hence, referring to Table *1*, four different specimens with the same nominal geometry and dimensions were printed using the following configurations: Fast-Coarse, Fast-Fine, Slow-Coarse, and Slow-Fine. Figure 1 shows one of the fabricated samples with the highest 3D printing quality (slow-fine), along with an internal view of the two pieces (upper and lower) showing the inner duct surface along the longitudinal sections. The overall thickness of the specimen is 11.1 mm, the diameter of the sample is $2R_0$ = 39 mm, the side of the hole square is 2a = 5.59 mm, the porosity of the front panel is ϕ = 2.6%, the total spiral length is L_t = 133 mm. PETG has a medium toxicity level, meaning that the environment where the printing machine is placed must be ventilated, or HEPA filters

installed in the automatically ventilated 3D printing machine. For the other 3D printing machines, MakerBot Replicator + was used to fabricate the PLA samples. The nozzle diameter used is 0.4 mm, and it travels at a printing speed of 60 mm/s on the base, 150 mm/s on the intermediate level, and 40 mm/s on the top and bottom solid layers. Each layer is printed with a Layer height of 0.2 mm and a Printing Temperature of 215°C (lower than the Flashforge Creator 3, which is 247°C). In this case, the Filling density is 10%. From the toxicity point of view, PLA is entirely non-toxic, and no specific training is required to manage this material for AM purposes.

Table 1 Constant and variable printing parameters. The combinations of two printing speed configurations (slow/fast) and two quality setting configurations (fine/coarse) are investigated through four distinct manufactured specimens.

Constant parameters	**Value**	
Extruder temperature (°C)	225	
Platform temperature (°C)	80	
Infill	Gyroid (3D infill)	
Infill density (%)	30	
Retraction (mm/s)	30	
Retraction Distance (mm)	2	
Number of outlines	4	
Support	No	
Raft	No	
Variable parameters	**Values**	
Printing Speed	**Slow**	**Fast**
Base speed (mm/s)	50	80
Outline speed (mm/s)	15	25
Solid layer speed (mm/s)	30	50
Infill speed (mm/s)	45	75
Quality setting	**Fine**	**Coarse**
N. of top and bottom solid layers	4	2
Layer height (mm)	0.12	0.30

2. SLA Set-up

Stereolithography (SLA) is a method that was created initially for technical prototyping tools related to the medical research environment (Dzionk, 2013; Lindén and Jakubiak, 2001) due to the reproduction precision at the μm scale (Dzionk, 2013; Rodriguez et al., 2021). For the same reasons, in recent years, bio-engineering and engineering researchers have been exploiting this method too, studying and characterising the SLA products from the physical, mechanical and environmental points of view(Bernasconi et al., n.d.; Rodriguez et al., 2021). SLA applications are also known in the metamaterial field (Casarini et al., 2018; Xiao et al., 2021; Yin et al., 2012) even though this is not the most preferred prototyping method, as it is more expensive than FDM, it needs more post-processing work and space, and the materials involved in this technology can result in toxic if not appropriately managed. For this specific AMM design, for example, after the solidification of the resin, SLA samples must undergo a post-processing cleaning of the inner duct to ensure that none of the liquid resin is left inside the coil, increasing the production time of each sample. So, in this research, SLA was considered to compare its products' quality with FDM in terms of accuracy in reproducing the expected acoustic performance according to analytical and numerical analysis. Due to the significantly higher accuracy in the geometry reproduction, the optimal printing parameters were already known for SLA (with both the elastic and non-elastic resins). They included a Printing speed of 30 s/layer, considering a 0.1 mm layer height, and a filling density of the geometrical voids of 100%. In this AM technology, the Printing speed is referred to the polymerisation of the liquid resin through UV light. The printer model was a DWS X-FAB; the polymers used were INVICTA 977 (non-flexible sample) and TDS IT_FLEXA693 (flexible sample). The resins used in SLA technology are commonly fairly toxics, and the post-processing materials (i.e. isopropyl alcohol) pose fire hazards. Therefore, an adequate working station is required and the staff managing the machine must be appropriately trained and use protection tools.

3. SLM Set-up

The Stainless Steel prototype was realised through Selective Laser Melting (SLM) additive 3D metal printing technology using an AISI 316L grade stainless steel powder with an EOS M280 3D printing machine. This AM technology involves a fast-moving laser which selectively melts the powder bed along its path. The laser has a rated power of 360W and a rated diameter of 50 μm with an Energy Density of 130J/m^3. The AISI 316L grade stainless steel powder is made of 30-40 μm diameter grains, and it can build with a layer height of 60μm with a specific weight of 7.98 g/cm^3. This technology is one of the most expensive, as it involves highly specialized equipment for metallic powder precise management and recycling, and is highly dangerous for human operators due to low diameter of metallic powders, which poses cancerogenic hazars. Dedicated and sealed environment are needed for storing the equipment, and operators need dedicated training and protective gear. with a specific weight of 7.98 g/cm^3. This technology is one of the most expensive , as it involves highly specialized equipment for metallic powder precise management and recycling, and is highly dangerous for human operators due to low diameter of metallic powders, which poses cancerogenic hazars. Dedicated and sealed environment are needed for storing the equipment, and operators need dedicated training and protective gear.

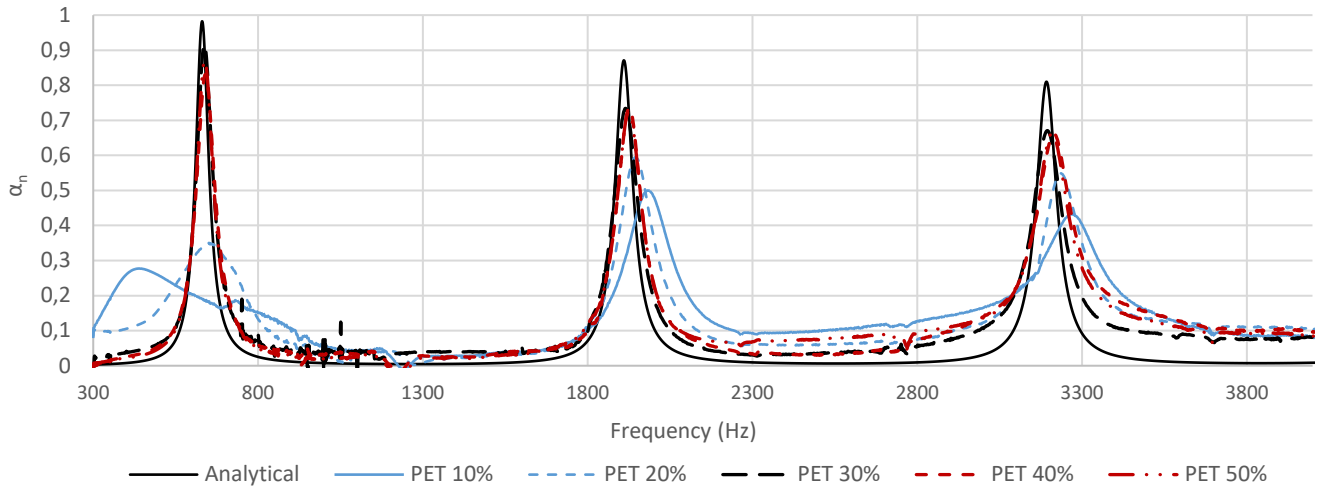

Figure 7 (Colour online) Normal incidence sound absorption coefficient of the PLA, and Stainless Steel samples, calculated and measured in the impedance tube of laboratories A and B.

III. RESULTS AND DISCUSSION

A. Sound absorption coefficient from different AM technologies and materials

Figure and Figure show the normal incidence sound absorption coefficient measured by the two labs in the frequency range of 300-4000 Hz. Overall, there is a significant correspondence between the values measured on the SLA and FDM PET samples (Figure 8) compared to the expected analytical result, while the PLA and Stainless Steel prototype results are not agreeing. Therefore, since the input geometry is the same for all the samples, it is probable that there are some non-optimised printing set-ups which increase the error between the expected analytical results and the experimental ones. The most disagreeing results are related to the Stainless Steel sample, which presents a single sound absorption coefficient peak around 1900 Hz (α_n = 0.95). Looking at the Stainless Steel sample section shown in Figure , bottom right, a significant occlusion of the internal duct due to Stainless Steel powder residuals is highlighted; therefore, the a_n curve of such a sample has one peak only in the given frequency range. The PLA analytical result in frequency and amplitude. However, from Figure 6, top left, no specific difference is highlighted in the geometric imperfections of the coiled duct, so further analysis of the roughness and the inner division wall characterisation could highlight details on the difference between the acoustic performance of PLA, PETG, and Resin samples.

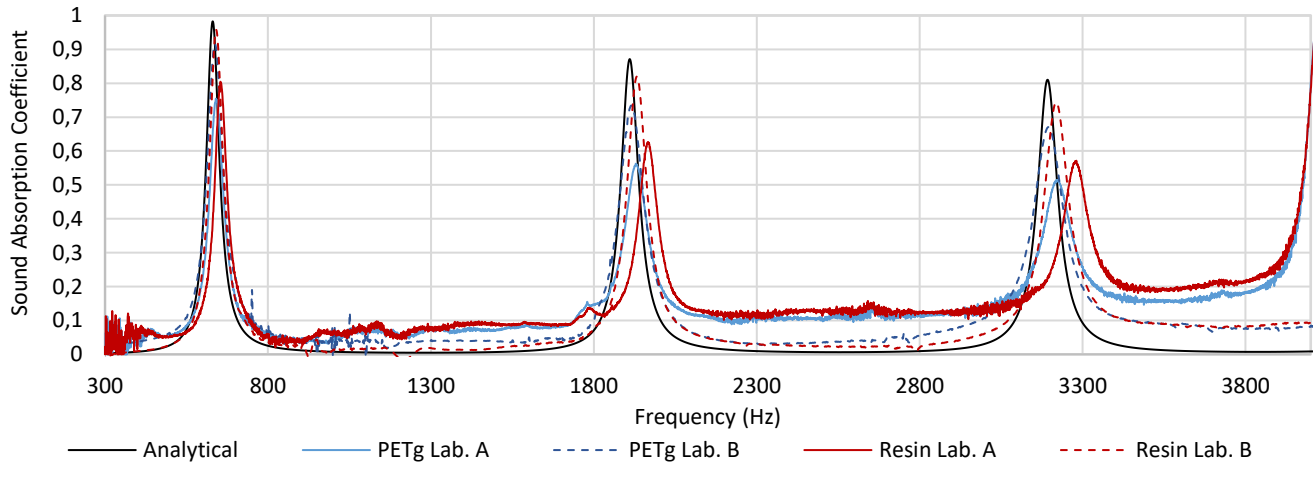

Figure 8 (Colour online) Normal incidence sound absorption coefficient of the PETG and Resin (including the arithmetical average of standard and flex resin results) samples, calculated and measured in the impedance tube of laboratories A and B.

B. Inner division wall characterisation through Roughness analysis

Table *2* shows the duct's internal surfaces' average roughness (Ra). In the FDM-made samples (PLA and PET), the upper layer, influenced by gravity, results significantly rougher than the bottom in all the measured samples (see Figure 6). On the other hand, the SLA/Resin samples have a more negligible difference between the upper and lower surface roughness, and overall, the R_a is smaller than that of the FDM samples. This is due to the absence of gravity-dependence of the UV polymerisation process used by SLA technology, making it the most precise in reproducing the AMM shape, even if more expensive, toxic, and has longer post-production times. As shown in Table *2*, the different internal roughness of PETG and Resin (either standard or flexible) samples determines mainly a slight alteration in the amplitude of the peaks (Figure 8), with a small shift of the peak frequency. Even if the duct's internal roughness can explain the difference between the acoustic performances of PLA, PETG, and Resin samples, it does not explain the differences between the two FDM samples' results. FDM samples differ mainly by the filling density (10% for PLA and 30% for PETG), which considers the percentage of filling material within the resulting geometrical volume of the 3D-printed samples. For this reason, a more in-depth analysis focusing on the 3D printing Filling Density is investigated in the next section.

C. Influence of Filling density over acoustic properties

Figure shows the sections of four samples where the resulting geometrical volumes are highlighted in red. The filling density in these volumes can be customised in the FDM set-up, while for the SLA, it is set as 100% by default: the SLA involves the solidification of liquid resin, which fills the geometrical domain

Table 2 Arithmetic average height Roughness (R_a) of the internal duct upper and bottom surfaces for each AM technique and material used to realise the prototype.

3D printing method	R_a (µm)	
	upper	bottom
1 (PLA - FDM)	41.12	6.22
2 (PETG - FDM)	35.54	3.17
3 (Resin - SLA)	0.48	1.36
4 Stainless Steel (FDM)	23.28	35.76

entirely. Since this variable parameter may determine a significant variation in the acoustic performance, it is crucial to assess its influence on the difference between the experimental results from the expected ones (from the analytical and numerical design). For this reason, a final experimental analysis was run to determine the optimal filling density for FDM PETG-based samples, keeping a slow-fine set-up (as assessed in the previous section). The filling percentages considered were 10%, 20%, 30%, 40%, and 50%, while all the other printing set-ups were kept as for the previous experimental analysis (including Printing Quality=Fine and Velocity=Slow). From the results shown in Figure , the samples which experimentally present higher correspondence with the analytical curve are those having a filling density of 30%, 40%, and 50%, while those with 10% and 20% filling density exhibit a_n-peak too damped (especially in the lower frequency range).

D. Comparison tests for outlining optimal FDM PET printing velocity and quality

The influence of the FDM manufacturing process has been evaluated by measuring the variation of the experimental sound

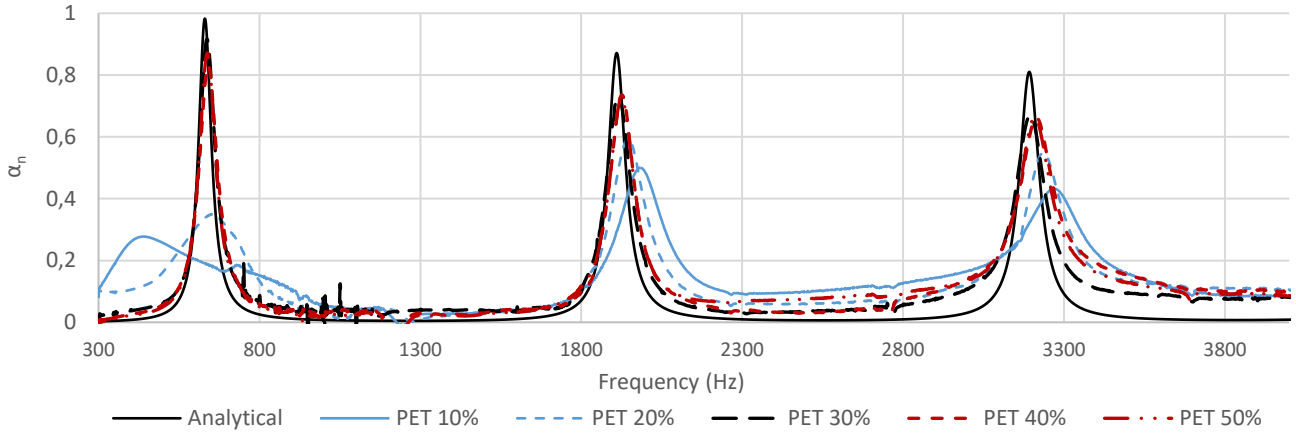

Figure 9 (Colour online) Comparison among the specimens fabricated with the five filling density settings (10%, 20%, 30%, 40%, 50% for PETG and 10%) and the prediction model.

absorption peak frequencies and amplitude from the analytical one. Figure 10 shows the first absorption peak's behaviour relative to four specimens fabricated with the 3D printing speed and coarse/fine quality setting. It should be noted that each specimen has been mounted and measured inside the impedance tube five times, so, in Figure , the average curve of five successive measurements is displayed, aiming to reduce the non-idealities effect and obtain a more reliable fitting with the model (Prato et al., 2021).

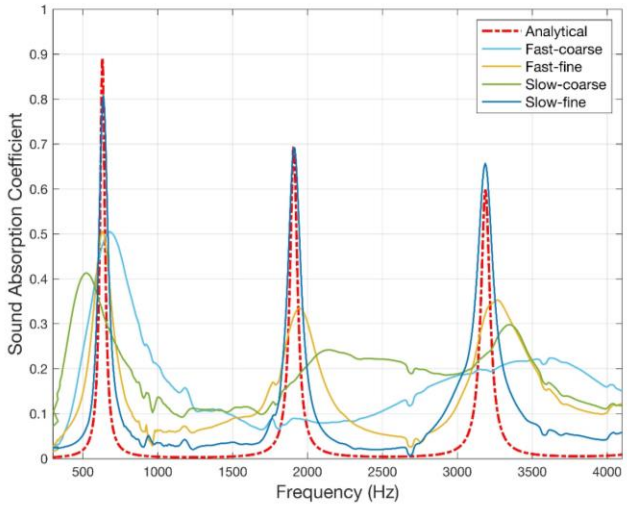

Figure 10 (Colour online) Comparison among the specimens fabricated with the four manufacturing settings and the predictive analytical model: the slow-fine setting best matches the prediction model. The RMS deviations of the four curves from the analytical model are: 27% for fast-coarse, 21% for fast-fine, 30% for slow-coarse, 14% for slow-fine.

Root-mean-square (RMS) deviations have been calculated to quantify the discrepancies between each configuration and the analytical model: 27% for fast-coarse, 21% for fast-fine, 30% for slow-coarse, 14% for slow-fine. Observing these experimental results, it is evident that these printing parameters significantly affect the acoustic performance of the specimens and the agreement with the theoretical values. Therefore, the quality setting (fine/coarse) influences more than the printing speed (slow/fast), and to understand why a qualitative analysis on the inner division wall characterisation (see Figure 6) was run through SEM technology. As shown in Figure 11.a,b, Printing Velocity determines an undulatory distribution of the filament layers overlapping in the internal wall when set as Fast, differently from the Slow one, which determines a linear distribution of overlapped layers. On the other side, Figure 11.c,d shows how the Printing Quality significantly varies the porosity between two layers of the wall when Coarse Printing Quality is involved. Therefore, as anticipated in Section II.E.1, the quality setting depends on the height of the layers: therefore, the finer the layers, the more accurate the inner division wall (between the solid and coiled duct) will be, and less porosity will appear on the limit surface between layers. Specifically, the average of pore diameter for Coarse setup is 7 μm. The internal total height of the resonant cavity section is 2a = 5.59 mm, while the length is 133.1mm. The number of layers for Fine setting is 50, while for Coarse is 20. Considering a superficial Coarse sample of a total area At=31.25 mm^2 and an average pore area of 0.49 μm^2, 429 pores can be count in one connecting surface between two layers 5.59mm long (see Figure 11.c). Therefore, for 18 overall connecting layers, a total of 7722 pores is contained averagely in 31.25mm^2, with a total Area of the pores (Ap) of 0.0038mm^2. Therefore, a 0.01% porosity can be considered in the internal division wall of the Coarse samples (being Pt=Ap/At=0.012%) which eventually combined with the empty volumes (determined by the filling density of 30%) could lead to the broadening of the α_n frequency range and decrease the peak's amplitude (see Figure 10, Slow-Coarse).

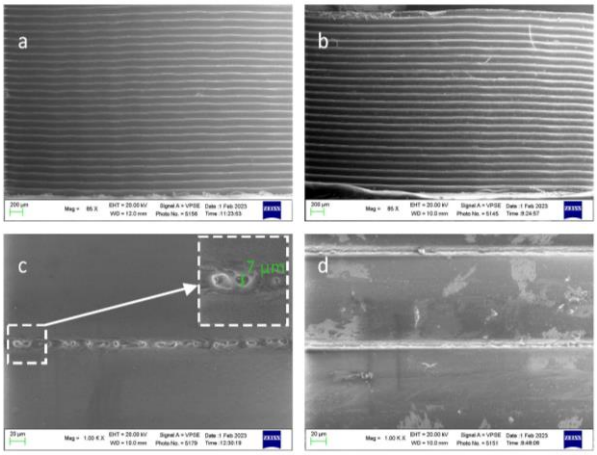

Figure 11 SEM scan which highlights within the inner division layer (a) undulatory layers in the internal (Fast printing Velocity), (b) linear layers (Slow printing Velocity), (c) porosity between layers (Coarse printing Quality), and (d) smooth layers (Fine printing Quality).

IV. CONCLUSION

In this paper, the influence of a specific 3D printing set-up on the acoustic performance of an exemplary sample - a coiled-up resonator – is studied, with the aim of finding the printing method that allows the best match of the experimental results with the expected analytical and numerical ones. In the first step, two Italian laboratories' experimental results were compared to determine which combination of printing techniques (FDM, SLA, and SLM) and material (PLA, PETG, Resin, Flexible Resin, and Stainless Steel) is the most effective for accurate reproduction of the expected acoustic performance. Considering the internal measured roughness, SLA performed overall better than the other samples (results in Table *2* show an overall R_a of 0.91 μm), followed by FDM

PETG (overall R_a of 19.36 μm). FDM PLA and Stainless Steel samples approximate the expected result with low resolution due to a relatively high internal duct roughness (respectively 23.67 μm and 29.52 μm). However, the roughness could not justify the differences found among the sound absorption coefficient peaks, as both FDM techniques had a R_a with a slight difference (ΔR_a = 4.31 μm) compared to the difference with SLA (ΔR_a = 22.75 μm).

On the other hand, filling density of 30% and above proved to reach the best approximation with the attended results in FDM technologies; this highlights the importance of characterising the resulting geometrical volumes within the 3D printed samples for their acoustic performance (16% of RMS deviation). For this reason, a further analysis was performed on other set-up parameters, such as printing Speed and Quality settings. As a result, an optimal printing configuration was found at a Slow-Fine printing set-up with a 14% RMS deviation from the attended result. Therefore, even if FDM PETG represents a cheaper and less refined sample, it can achieve the same acoustic performance as the SLA Resin (which is more expensive and needs much more post-processing), selecting the optimal printing set-up.

Our parametric and comparative study determined an optimal and affordable 3D printing set-up and material choice for producing coiled-up resonators that better approximate the analytical and numerical designed result. It is hoped that the methodology applied to this prototype could be extended to other AMMs in further studies.

V. Acknowledgement

This research was funded by the Ministero dell'Istruzione dell'Università della Ricerca (Italy), within the project PRIN 2017, grant number 2017T8SBH9: "Theoretical modelling and experimental characterisation of sustainable porous materials and acoustic metamaterials for noise control".

The authors would also like to thank Maria Giulia Faga and Giovanni Gautier from CNR STEMS (Torino, Italy) for their availability to measure the roughness of the tested materials with their roughness tester.

References

Allen, R. J. A., and Trask, R. S. (**2015**). "An experimental demonstration of effective Curved Layer Fused Filament Fabrication utilising a parallel deposition robot," Addit. Manuf., **8**, 78–87. doi:10.1016/J.ADDMA.2015.09.001

Alomarah, A., Masood, S. H., and Ruan, D. (**2022**). "Metamaterials with enhanced mechanical properties and tuneable Poisson's ratio.," Smart Mater. Struct., **31**, 025026.

Askari, M., Hutchins, D. A., Thomas, P. J., Astolfi, L., Watson, R. L., Abdi, M., Ricci, M., et al. (**2020**). "Additive manufacturing of metamaterials: A review," Addit. Manuf., , doi: 10.1016/J.ADDMA.2020.101562. doi:10.1016/J.ADDMA.2020.101562

Assouar, B., Liang, B., Wu, Y., Li, Y., Cheng, J.-C., and Jing, Y. (**2018**). "Acoustic metasurfaces," Nat. Rev. Mater., **3**, 460–472. doi:10.1038/s41578-018-0061-4

Bernasconi, R., Credi, C., Tironi, M., Levi, M., and Magagnin, L. (**n.d.**). "Electroless Metallization of Stereolithographic Photocurable Resins for 3D Printing of Functional Microdevices," J. Electrochem. Soc., **164**, B3059–B3066. doi:10.1149/2.0081705jes

Cai, X., Guo, Q., Hu, G., and Yang, J. (**2014**). "Ultrathin low-frequency sound absorbing panels based on coplanar spiral tubes or coplanar Helmholtz resonators," Appl. Phys. Lett., **105**, 121901. doi:10.1063/1.4895617

Casarini, C., Tiller, B., Mineo, C., MacLeod, C. N., Windmill, J. F. C., and Jackson, J. C. (**2018**). "Enhancing the Sound Absorption of Small-Scale 3-D Printed Acoustic Metamaterials Based on Helmholtz Resonators," IEEE Sens. J., **18**, 7949–7955. doi:10.1109/JSEN.2018.2865129

Chen, J. S., Chen, Y. Bin, Cheng, Y. H., and Chou, L. C. (**2020**). "A sound absorption panel containing coiled Helmholtz resonators," Phys. Lett. Sect. A Gen. At. Solid State Phys., , doi: 10.1016/J.PHYSLETA.2020.126887. doi:10.1016/J.PHYSLETA.2020.126887

Chung, J. Y., and Blaser, A. (**1998**). "Transfer function method of measuring in-duct acoustic properties. II. Experiment," J. Acoust. Soc. Am., **68**, 914. doi:10.1121/1.384779

Cingolani, M., Fusaro, G., Fratoni, G., and Garai, M. (**2022a**). "Influence of thermal deformations on sound absorption of three-dimensional printed metamaterials," JASA, , doi: 10.1121/10.0011552. doi:10.1121/10.0011552

Cingolani, M., Fusaro, G., and Garai, M. (**2022b**). "The influence of thermo-hygrometric conditions on metamaterials ' acoustic performance : an investigation on a 3-D printed coiled-up resonator," Internoise, Glasgow.

Corredor-Bedoya, A. C., Acuña, B., Serpa, A. L., and Masiero, B. (**2021**). "Effect of the excitation signal type on the absorption coefficient measurement using the impedance tube," Appl. Acoust., , doi: 10.1016/J.APACOUST.2020.107659. doi:10.1016/J.APACOUST.2020.107659

Dzionk, S. (**2013**). "Surface structure of components created by stereolitography," Solid State Phenom., **199**, 338–343. doi:10.4028/www.scientific.net/SSP.199.338

Encyclopedia Britannica, (**n.d.**). Available: https://www.britannica.com/. Retrieved from https://www.britannica.com/

Franco-Martínez, F., Grasl, C., Kornfellner, E., Vostatek, M., Cendrero, A. M., Moscato, F., Andrés, &, et al. (**2022**). "Hybrid design and prototyping of metamaterials and metasurfaces," , doi: 10.1080/17452759.2022.2101009. doi:10.1080/17452759.2022.2101009

Fusaro, G., Yu, X., Kang, J., and Cui, F. (**2020**). "Development of metacage for noise control and natural ventilation in a window system," Appl. Acoust., **170**, 107510. doi:10.1016/j.apacoust.2020.107510

Gadelmawla, E. S., Koura, M. M., Maksoud, T. M. A., Elewa, I. M., and Soliman, H. H. (**2002**). "Roughness parameters," J. Mater. Process. Technol., **123**, 133–145. doi:https://doi.org/10.1016/S0924-0136(02)00060-2]

Helmholtz, H. von (**1863**). *Die Lehre von den Tonempfindungen als physiologische Grundlage für die Theorie der Musik [The Study of the Sensations of Tone as a Physiological Foundation for Music Theory]*, 1 ed.

ISO 10534-2: 1998. Acoustics – Determination of sound absorption coefficient and impedance in impedance tubes – Part 2: Transfer function method (**1998**). International Organisation for Standardisation.

ITA-Toolbox (**2017**). "ITA-Toolbox, Open source MATLAB toolbox for acoustics developed by the Institute of Technical Acoustics of the RWTH Aachen University.,"

Jimenez, N., Cox, T. J., Romero-Garcia, V., and Groby, J. P. (**2017**). "Metadiffusers: Sound diffusers with deep-subwavelength dimensions," 2017 11th Int. Congr. Eng. Mater. Platforms Nov. Wave Phenomena, Metamaterials 2017, , doi: 10.1109/MetaMaterials.2017.8107876. doi:10.1109/MetaMaterials.2017.8107876

Jiménez, N., Huang, W., Romero-García, V., Pagneux, V., and Groby, J.-P. P. (**2016**). "Ultra-thin metamaterial for perfect and quasi-omnidirectional sound absorption," Appl. Phys. Lett., **109**, 121902. doi:10.1063/1.4962328

Johnston, W., and Sharma, B. (**2021**). "Additive manufacturing of fibrous sound absorbers," Addit. Manuf., **41**, 101984. doi:10.1016/j.addma.2021.101984

Kennedy, J., Flanagan, L., Dowling, L., Bennett, G. J., Rice, H., Trimble, D., and Groby, J.-P. (**2019**). "The Influence of Additive Manufacturing Processes on the Performance of a Periodic Acoustic Metamaterial," , doi: 10.1155/2019/7029143. doi:10.1155/2019/7029143

Kim, D. H., and Yoon, G. H. (**2021**). "Active acoustic absorption device using additive manufacturing technique for normal incident wave," Appl. Acoust., , doi: 10.1016/J.APACOUST.2021.108006. doi:10.1016/J.APACOUST.2021.108006

Kuznetsov, V. E., Solonin, A. N., Urzhumtsev, O. D., Schilling, R., and Tavitov, A. G. (**2018**). "Strength of PLA Components Fabricated with Fused Deposition Technology Using a Desktop 3D Printer as a Function of Geometrical Parameters of the Process," , doi: 10.3390/polym10030313. doi:10.3390/polym10030313

Ligon, S. C., Liska, R., Stampfl, J., Gurr, M., and Mülhaupt, R. (**2017**). "Polymers for 3D Printing and Customized Additive Manufacturing," Chem. Rev., **117**, 10212–10290. doi:10.1021/acs.chemrev.7b00074

Lindén, L. A., and Jakubiak, J. (**2001**). "Three-dimensional (3D) photopolymerization in the stereolitography. Part III. Medical applications of laser-induced photopolymerization and 3D stereolithography," Polimery/Polymers, **46**, 227–231. doi:10.14314/polimery.2001.227

Lu, Z., Yu, X., Lau, S. K., Khoo, B. C., and Cui, F. (**2020**). "Membrane-type acoustic metamaterial with eccentric masses for broadband sound isolation," Appl. Acoust., **157**, 107003. doi:10.1016/j.apacoust.2019.107003

Magnani, A., Marescotti, C., and Pompoli, F. (**2022**). "Acoustic absorption modeling of single and multiple coiled-up resonators," Appl. Acoust., , doi: 10.1016/J.APACOUST.2021.108504. doi:10.1016/J.APACOUST.2021.108504

Marburg, S., and Nolte, B. (**2008**). *Computational Acoustics of Noise Propagation in Fluids: Finite and Boundary Element Methods*, Springer, New York, 578 pages.

Matlab (**2019**). "MATLAB Version 9.6.0.1072779 (R2019a).,"

Melnikov, A., Maeder, M., Friedrich, N., Pozhanka, Y., Wollmann, A., Scheffler, M., Oberst, S., et al. (**2020**). "Acoustic metamaterial capsule for reduction of stage machinery noise," J. Acoust. Soc. Am., **147**, 1491–1503. doi:10.1121/10.0000857

Morris, C., Bekker, L., Haberman, M. R., and Seepersad, C. C. (**2018**). "Design exploration of reliably manufacturable materials and structures with applications to negative stiffness metamaterials and microstereolithography1," J. Mech. Des. Trans. ASME, , doi: 10.1115/1.4041251. doi:10.1115/1.4041251

Pilch, A. (**2021**). "Optimized diffusers for shoe-box shaped performance halls," Appl. Acoust., **178**, 108019. doi:10.1016/j.apacoust.2021.108019

Prato, A., Schiavi, A., Pandolfi, T., Corona, D., and Fasana, A. (**2021**). "Uncertainty of impedance tube sound absorption measurements of a spiral-tube-shaped 3-D printed acoustic metamaterial," "Advances Acoust. Noise Vib. - 2021" Proc. 27th Int. Congr. Sound Vib. ICSV 2021,.

Rodriguez, N., Ruelas, S., Forien, J. B., Dudukovic, N., Deotte, J., Rodriguez, J., Moran, B., et al. (**2021**). "3D printing of high viscosity reinforced silicone elastomers," Polymers (Basel)., , doi: 10.3390/polym13142239. doi:10.3390/polym13142239

Shao, C., Xiong, W., Long, H., Tao, J., Cheng, Y., and Liu, X. (**2021**). "Ultra-sparse metamaterials absorber for broadband low-frequency sound with free ventilation," J. Acoust. Soc. Am., **150**, 1044–1056. doi:10.1121/10.0005850

Standardization, I. O. for (**2021**). *, Geometrical product specifications (GPS) — Surface texture: Profile — Part 2: Terms, definitions and surface texture parameters*.

Stinson, M. R., and Champoux, Y. (**1992**). "Propagation of sound and the assignment of shape factors in model porous materials having simple pore geometries," J. Acoust. Soc. Am., **91**, 685–695. doi:10.1121/1.402530

Sutton, A. P. (**2021**). *Concepts of Materials Science*, Oxford University Press.

Varanasi, S., Bolton, J. S., and Siegmund, T. (**2017**). "Experiments on the low frequency barrier characteristics of cellular metamaterial panels in a diffuse sound field," J. Acoust. Soc. Am., **141**, 602–610. doi:10.1121/1.4974257

Wang, X., Zhao, H., Luo, X., and Huang, Z. (**2016**). "Membrane-constrained acoustic metamaterials for low frequency sound insulation," Appl. Phys. Lett., **108**, 1–6. doi:10.1063/1.4940717

Xiao, R., Ding, M., Wang, Y., Gao, L., Fan, R., and Lu, Y. (**2021**). "Stereolithography (SLA) 3D printing of carbon fiber-graphene oxide (CF-GO) reinforced polymer lattices," , doi: 10.1088/1361-6528/abe825. doi:10.1088/1361-6528/abe825

Yin, M., Tian, X. Y., and Han, H. X. (**2012**). "Free-space carpet-cloak based on gradient index photonic crystals in metamaterial regime," Cite as Appl. Phys. Lett, **100**, 124101. doi:10.1063/1.3696040

Yu, X., Lu, Z., Liu, T., Cheng, L., Zhu, J., and Cui, F. (**2019**). "Sound transmission through a periodic acoustic metamaterial grating," J. Sound Vib., **449**, 140–156. doi:10.1016/j.jsv.2019.02.042

Zhu, Y., Fan, X., Liang, B., Cheng, J., and Jing, Y. (**2017**).

"Ultrathin acoustic metasurface-based schroeder diffuser," Phys. Rev. X, **7**, 1–11. doi:10.1103/PhysRevX.7.021034

Zieliński, T. G., Opiela, K. C., Pawłowski, P., Dauchez, N., Boutin, T., Kennedy, J., Trimble, D., et al. (**2020**). "Reproducibility of sound-absorbing periodic porous materials using additive manufacturing technologies: Round robin study," Addit. Manuf., , doi: 10.1016/j.addma.2020.101564. doi:10.1016/j.addma.2020.101564